C: Surfaces, Interfaces, Porous Materials, and Catalysis

Contact Angle and Condensation of a CO Droplet on a Solid Substrate

Jianyang Wu, Asmund Ervik, Ingrid Snustad, Senbo Xiao, Amy L. Brunsvold, Jianying He, and Zhiliang Zhang

J. Phys. Chem. C, **Just Accepted Manuscript** • DOI: 10.1021/acs.jpcc.8b08927 • Publication Date (Web): 07 Dec 2018

Contact Angle and Condensation of a CO_2 Droplet on a Solid Surface

Jianyang Wu,[1,2,*] Åsmund Ervik,[3] Ingrid Snustad,[1] Senbo Xiao,[1] Amy Brunsvold,[3] Jianying He[1] and Zhiliang Zhang[1,*]

[1]NTNU Nanomechanical Lab, Norwegian University of Science and Technology (NTNU), Trondheim 7491, Norway

[2]Department of Physics, Research Institute for Biomimetics and Soft Matter, Jiujiang Research Institute and Fujian Provincial Key Laboratory for Soft Functional Materials Research, Xiamen University, Xiamen 361005, PR China

[3]SINTEF Energy Research, P. O. Box 4761 Sluppen, Trondheim 7465, Norway

Abstract: Anthropogenic release of carbon dioxide (CO_2) is a major contribution to manmade increase in global warming. Carbon Capture and Storage (CCS) is a necessary technology for lowering CO_2 emissions to an acceptable level that limits global warming to below 2 degrees. Liquefaction of CO_2 is a key process both in capture technologies and in conditioning before ship transport. The efficiency of this process can be remarkably enhanced by promoting dropwise CO_2 condensation on cooling surfaces, yet this remains largely unexplored. Here, using molecular dynamics (MD) simulations, we report for the first time the contact angle and condensation behaviour of CO_2 droplets on a smooth solid surface. The contact angle of the condensed CO_2 droplet is greatly dependent on the CO_2-solid characteristic interaction energy, but this does not hold true for the sum of condensed molecules. In contrast, the sum of condensed molecules for the filmwise condensation regime increases monotonically at first, but then remains constant as the CO_2-solid interaction energy approaches to a critical value. It is also revealed that droplet condensation on a cooling surface shows three distinct stages that are primarily characterized by heterogeneous cluster nucleation, diffusion-coalescence, and Ostwald ripening-coalescence mechanisms. As the area of the solid surface is increased by diffusion-induced coalescence of clusters at the first stage, cluster nucleation proceeds but ceases in the last stage at which the sum of condensed molecules are not accumulated. Analysis of the Ostwald ripening kinetics of a CO_2 droplet reveals a constant growth rate of around 11 CO_2 molecules/ns of the droplet.

*Corresponding emails: jianyang@xmu.edu.cn, zhiliang.zhang@ntnu.no

1. Introduction

Carbon dioxide (CO_2) is one of the dominant gases contributing to the earth's greenhouse effect. Anthropogenic release of CO_2 from fossile sources contributes to an increased global warming, with potentially catastrophic consequences. Substantial reduction of CO_2 emissions from industrial processes such as power generation, steel and cement production, etc. by combustion of fossil fuels is necessary to restrain and reverse the global warming process. Beyond those negative impacts, however, CO_2 also finds versatile important applications, such as in fire extinguishers, as a safe refrigerant and coolant, used in the brewing of soft drinks, beers and other alcoholic drinks, for softening water to avoid corrosion, producing potable water, enhancing oil recovery (EOR), sand blasting, hardening of metal castings, and so forth [1-7]. Utilization of CO_2 as a byproduct not only provides significant economic benefits but can also in some cases mitigate global warming and climate change concerns. There is, thus, a rapid growth in both academic research activities and industrial research and development (R&D) programmes worldwide to explore solutions for controlling CO_2 emissions.

Carbon Capture and Storage (CCS) is considered as one of the most effective CO_2 emission abatement strategies to combat climate change migration [8-10]. Generally, there are three emerging pathways for CO_2 capture, including pre-combustion, post-combustion, and oxy-fuel processes [6-9, 11-12]. Among them, the post-combustion is well understood, has lower capital expenditure (CAPEX) and is favored for CO_2 capture projects in the short-term. To date, a variety of technologies has been emerged for post-combustion CO_2 capture, including adsorption, physical absorption, chemical absorption, cryogenics separation and membranes[13-16]. While these technologies are rapidly being matured for post-combustion power plants, the main drawback is the high-energy penalties that must be paid. Moreover, although the aqueous organic amine-based method is relatively mature for post-combustion CO_2 capture, this technology shows several drawbacks including toxicity, degradation, and evaporation of the solvent [10]. Recently, CO_2 capture by mineralization (CO_2 molecules react with

the cationic metal atoms in expandable clays to form carbonate minerals) was proposed and investigated[17-18].

Inspired by water or fog harvest by droplet condensation on hydrophobic-functionalized or patterned solid surfaces [19-22], a relatively novel CO_2 capture technology by dropwise CO_2 condensation on cooling surfaces has been recently envisaged [23]. Gaseous CO_2 is expected to condense as liquid droplets onto functionalized surfaces of heat exchangers that are cooled. An advantage of this conditioning process may enable a potentially improved low temperature capture technique and no chemical absorbents are needed. To date, researches on CO_2 condensation on solid surfaces are extremely rare [23-24], although there have been investigations on cooling of CO_2 that mainly concentrated on supercritical gas cooling and wettability of water on solid surfaces upon CO_2 pressure [25-33]. Understanding the fundamental wetting and condensation behaviours of CO_2 on a cooling surface is a necessary starting point for CO_2 capture by the technology. Molecular dynamics (MD) simulation has become an indispensable tool for investigating details of water condensation, wettability and nucleation on functionalized and patterned solid surfaces [34-42]. Since experimental measurements of the contact angle of liquid CO_2 on functionalized surfaces currently under development are yet to be performed, the interaction energy between the CO_2 and substrate is considered as a free parameter in this work, spanning the range of contact angles. The functionalized surfaces are likely to be made from (or contain a high percentage of) copper, due to the excellent heat transfer properties of this material, and thus we consider a copper substrate. In this work, we present, for the first time, the contact angle and condensation of CO_2 on cooling solid surface by large-scale MD simulations.

2. Methods

All the MD simulations are implemented by the LAMMPS MD simulation package. A many-body interatomic potential of embedded-atom method (EAM) derived by Mishin et al.[43] is adopted to model

the interatomic interactions in a face-cubic-center (fcc) copper (Cu) surface with a (1 0 0) surface. In this EAM forcefield[44], the total potential energy of an elemental system is given by

$$E = \frac{1}{2}\sum_{ij} U\left(r_{ij}\right) + \sum_{ij} F\left(\overline{\rho_i}\right) \tag{1}$$

where

$$\overline{\rho}_i = \sum_{j \neq i} \rho\left(r_{ij}\right) \tag{2}$$

Here $U\left(r_{ij}\right)$ is a pair-wise potential as a function of distance (r_{ij}) between atom *i* and atom *j*. $F\left(\overline{\rho_i}\right)$ is the embedding energy required to place an atom into the host electron density $\overline{\rho_i}$ that is the sum of the contributions $\rho\left(r_{ij}\right)$ from all the other atoms in the system.

The pairwise potential function is expressed as

$$\begin{aligned} U\left(r\right) = &\left[E_1 M\left(r, r_0^{(1)}, \alpha_1\right) + E_2 M\left(r, r_0^{(2)}, \alpha_2\right) + \delta\right] \\ &\times \psi\left(\frac{r - r_c}{h}\right) - \sum_{n=1}^{3} H\left(r_s^{(n)} - r\right) S_n \left(r_s^{(n)} - r\right)^4 \end{aligned} \tag{3}$$

where

$$M\left(r, r_0, \alpha\right) = \exp\left[-2\alpha\left(r - r_0\right)\right] - 2\exp\left[-\alpha\left(r - r_0\right)\right] \tag{4}$$

$$\psi\left(x\right) = \begin{cases} 0, & x \geq 0 \\ \dfrac{x^4}{x^4 + 1}, & x < 0 \end{cases} \tag{5}$$

are a Morse function and a cutoff function, respectively. The embedding function is written as

$$F\left(\overline{\rho}\right)=\begin{cases} F^{(0)}+\frac{1}{2}F^{(2)}\left(\overline{\rho}-1\right)^{2}+\sum_{n=1}^{4}q_{n}\left(\overline{\rho}-1\right)^{n+2}, & \overline{\rho}\le 1 \\ \dfrac{F^{(0)}+\frac{1}{2}F^{(2)}\left(\overline{\rho}-1\right)^{2}+q_{1}\left(\overline{\rho}-1\right)^{3}+Q_{1}\left(\overline{\rho}-1\right)^{4}}{1+Q_{2}\left(\overline{\rho}-1\right)^{3}}, & \overline{\rho}>1 \end{cases} \tag{6}$$

The potential is capable to reproduce various properties of Cu, such as lattice properties, elastic constants, thermal expansion, point and extended defects, and epitaxial growth of Cu films on (0 0 1)-oriented *fcc* or body-centered-cubic (bcc) substrates[43]. For the CO_2 modelling, the efficient and accurate coarse-grained (CG) forcefield of SAFT-γ Mie potential is used for the intermolecular interactions of CO_2. The functional form of CG SAFT-*γ Mie* potential is expressed as [45-46]

$$\phi^{\mathrm{Mie}}\left(r\right)=\varepsilon C\left(\lambda_{a},\lambda_{r}\right)\left[\left(\frac{\sigma}{r}\right)^{\lambda_{r}}-\left(\frac{\sigma}{r}\right)^{\lambda_{a}}\right] \tag{7}$$

where

$$C\left(\lambda_{a},\lambda_{r}\right)=\left(\frac{\lambda_{r}}{\lambda_{r}-\lambda_{a}}\right)\left(\frac{\lambda_{r}}{\lambda_{a}}\right)^{\beta}\ \text{with}\ \beta=\left(\frac{\lambda_{a}}{\lambda_{r}-\lambda_{a}}\right) \tag{8}$$

where r, ε and σ are the intermolecular distance, the depth of the potential well and the diameter of the CO_2 CG bead, respectively. λ_r and λ_a are the repulsive and attractive exponents of the molecular bead-bead interactions which characterize the pair energy. The SAFT-*γ Mie* forcefield parameters σ, λ_r and λ_a are 3.741 Å, 23.0 and 6.66 for CG CO_2 bead, respectively [45]. The diameter of the CO_2 CG bead is similar to the lattice constant of *fcc* Cu. The *Mie* potential is also adopted to describe the interaction between CO_2 molecules and Cu-like solid surface. The energy interaction parameter $\varepsilon_{CO_2\text{-}Cu}$ varies from 0.001-0.1 eV to fully cover the surface properties of a solid-surface from CO_2-phobic to

CO_2-philic. The main purpose of using Cu substrate is to provide a physical solid state for CO_2 to adsorb. By varying the energy interaction parameter between CO_2 and the substrate, the MD simulations can qualitatively predict CO_2 adsorbing dynamics and possibly equilibrium contact angles on the substrates with different surface energies. For the sake of simplicity, the internal interactions between the substrate atoms, namely Cu atoms, were kept the same in all the simulations for maintaining the integrity of the substrate, and to provide constant surface structure. In reality, it is only possible to use other atom types, for instances, Fe, Al or Au, to provide different energy interaction parameter ε between CO_2 and the flat substrate. Yet, different atoms types will result in different surface lattice structure and size, which are also important factors for CO_2 condensation. Such complexity is beyond the scope of the current study. The cutoff distance of 15 Å is utilized for the CG *Mie* potential interactions. The velocity-Verlet method is employed to integrate the equation of atomic motions with a timestep of 10 fs in all cases.

3. Results and discussion

To validate the implemented SAFT-γ Mie model of CO_2, the temperature-density vapor-liquid equilibria (VLE) curve is studied. A slab consisting of 18450 CO_2 molecules is initially placed in the center of an otherwise empty simulation box with dimensions of 92 Å × 92 Å × 500 Å. The system is then fully equilibrated in an NVT ensemble with sufficient simulation time of 10 ns to achieve a stable liquid film in equilibrium with its vapor phase, as shown in Figure 1a. Figure 1b presents the density profiles obtained by averaging over the last 20000 timesteps in the vapor-liquid system at temperatures ranging from 220 K - 290 K. Each bin is set in 2.5 Å for calculating the density of CO_2. Similar to previous studies, the density profiles of local vapor-liquid interface can be well-fitted by both tangent hyperbolic and error functions [47-48] that are respectively written as

$$\rho(z) = \frac{1}{2}(\rho_l + \rho_v) - \frac{1}{2}(\rho_l - \rho_v)\tanh\left[\frac{2}{d}(z-1)\right] \quad (9)$$

and

$$\rho(z) = \frac{1}{2}(\rho_l + \rho_v) - \frac{1}{2}(\rho_l - \rho_v)\,\mathrm{erf}\left[\frac{\sqrt{\pi}}{d}(z-1)\right] \quad (10)$$

where ρ_l and ρ_v are the densities of liquid and vapor in equilibrium, respectively. *l* and *d* are the middle-position of the equilibrium vapor-liquid interface and the thickness parameter, respectively. As expected, the liquid density and the number of molecules in the liquid CO_2 declines with increasing temperature, while the vapor density increases. This suggests that, upon cooling, vapor of CO_2 tends to condense on the liquid slab to balance the vapor-liquid equilibrium. Figure 1c compares the predicted vapor-liquid coexistence densities of CO_2 by MD simulation with those calculated using the Span-Wagner (SW) equation of state (EoS) with the methodology given in Ref. 46. There is a good agreement between the MD simulation and SW EoS for the temperature-density distribution of CO_2 phase diagram [49-50]. This confirms that the SAFT-γ CG Mie model of CO_2 is correctly implemented and this model is able to predict the bulk thermodynamic properties [45]. Other works have verified that the model also yields accurate predictions the vapor-liquid interfacial behaviour for the CO_2 molecules [51-52].

With accurate models for the CO_2 and the surface, we proceed to study the evolution of a CO_2 nanodroplet on a Cu-like smooth solid surface. An initial CO_2 cubic box containing 43537 CO_2 CG beads is placed on the Cu-like flat surface with 2D planar dimensions of 400 Å × 400 Å. Within a sufficient equilibration simulation time of 50 ns at 223.15 K, the initially generated CO_2 box evolves to a mixture of vapor-liquid droplet or a mixture of vapor-liquid film, depending on surface wettability. In the simulations, there is no integration of motion for the Cu-like solid surface. The coordinates of each beads are collected in every 100 ps for monitoring the development of the CO_2 droplet, and the density contours of CO_2 are obtained by taking samples of the dynamic droplet at every 10000 timesteps for the last simulation of 1 ns. Figure 2 shows the calculated 2D density contours of the CO_2 droplet on Cu-like surface (z = 10 Å) with different wettability. Apparently, liquid-state CO_2 molecules are more strongly attracted by a CO_2-philic Cu-like surface than by a CO_2-phobic Cu-like surface as

the solid-CO_2 characteristic energy is increased. Here, a symbol $\varepsilon_{CO_2\text{-}Cu}$ is used to denote the parameter of interaction between copper and CO_2. The range of $\varepsilon_{CO_2\text{-}Cu}$ from 0.001 to 0.015 eV is able to cover the surface wettability perfectly, changing from CO_2-phobic to CO_2-philic. As $\varepsilon_{CO_2\text{-}Cu}$ is 0.001 eV, a stable spherical CO_2-droplet is suspended in the vapor without contacting the Cu-like surface, indicating a perfect CO_2-phobicity (Figure 2a). When the $\varepsilon_{CO_2\text{-}Cu}$ varies from 0.003 to 0.012 eV, very clearly the shape of a CO_2 droplet on the Cu-like surface is identified (Figure 2b-g). As $\varepsilon_{CO_2\text{-}Cu}$ becomes larger ($\geq$ 0.015 eV), the Cu-like surface shows a perfect CO_2-philicity (Figure 2h). An inhomogeneity in the density of CO_2 in the droplet is identified, especially near the droplet and the Cu-like surfaces. Notably, the boundaries between liquid and gas phases of CO_2 are distinguished by the green-highlighted region in the relative density contour plots. In the vicinity of the Cu-like surface with $\varepsilon_{CO_2\text{-}Cu}$ ranging from 0.008 to 0.012 eV, formation of a four-layer CO_2 sheet with thickness of around 10.6 Å, separating the Cu-like solid surface and the rest of the droplet, is observed (Figure 2d-g). The thickness of each layer (2.65 Å) implies that the layers are monomolecular. The density of liquid CO_2 near the Cu-like surface declines as the layer is moving away from the Cu-like surface. For the Cu-like surface with higher CO_2-phobicity, the number of CO_2 layers near the Cu-like surface decreases (Figure 2b and c). With respect to the Cu-like surface with a perfect CO_2-philicity ($\varepsilon_{CO_2\text{-}Cu} = 0.015$ eV), an apparent CO_2 tri-layer is formed and the layer nearest to the Cu-like surface shows higher density than the other layers.

Figure 3a presents a representative equilibrium snapshot of a CO_2 droplet on the Cu-like surface ($\varepsilon_{CO_2\text{-}Cu} = 0.008$ eV). Unlike for a water droplet in air on a solid surface, the vapor and liquid here consist of the same fluid molecules, so the liquid droplet (blue) and vapor (yellow) of CO_2 coexist in the simulation system. The contact angle θ_c of a CO_2 droplet on the Cu-like surface is defined by the tangent at the contact line, as illustrated in Figure 2d. Figure 3b plots the calculated contact angle θ_c

of a CO_2 droplet as a function of the CO_2-surface interaction $\varepsilon_{CO_2\text{-}Cu}$. As expected, the contact angle is sensitive to the interaction energy $\varepsilon_{CO_2\text{-}Cu}$ between CO_2 molecules and the attractive surface. The contact angle monotonically decreases from 180˚ to 0˚ with $\varepsilon_{CO_2\text{-}Cu}$ increasing from 0.001-0.015 eV. Large $\varepsilon_{CO_2\text{-}Cu}$ > 0.015 eV leads to complete spreading of the CO_2 droplet and wetting of the solid surface. Particularly, an energy interaction parameter $\varepsilon_{CO_2\text{-}Cu}$ of 0.009 eV (the liquid-solid tension of around 10 mN/m) yields a contact angle of approximately 90˚ of a CO_2 droplet, which is the critical point for transition from CO_2-phobic to CO_2-philic. Figure 3c and 3d plot the number of liquid CO_2 molecules and the density of CO_2 vapor as a function of simulation time for different Cu-like surface wettability. For all our studied systems with different wettability of surfaces, two stages in the curves can be roughly identified. The first stage is characterized by a monotonic reduction in number of liquid molecules or an increase in density of the CO_2 vapor. This quantitatively illustrates the vaporization process of liquid CO_2. The initial vaporization rate is closely related to the energy interaction parameter $\varepsilon_{CO_2\text{-}Cu}$. For an energy interaction parameter $\varepsilon_{CO_2\text{-}Cu}$ between 0.001 and 0.02 eV, a small difference in the initial vaporization rate is observed. When it is > 0.02 eV, however, the initial vaporization rate shows a decreasing trend. Moreover, the vaporization rate declines with the simulation time. The second stage corresponds to the long plateau in the curves. This indicates the vapor-liquid equilibrium for CO_2 contacting a Cu-like surface. Figure 3e and 3f plot the equilibrated number of liquid CO_2 molecules and the CO_2 vapor density, respectively, as function of the energy interaction parameter $\varepsilon_{CO_2\text{-}Cu}$, respectively. Intriguingly, for the energy interaction parameter $\varepsilon_{CO_2\text{-}Cu}$ yielding a non-zero contact angle of a droplet, there is a negligible difference in the total number of CO_2 molecules in liquid-state. As the solid surface becomes more CO_2-philic, however, the number of liquid CO_2 molecules increases pronouncedly. This is because more CO_2 molecules are attracted by the Cu-like surface with strong attractive interaction. Notably, the number of liquid CO_2 molecules remains constant as the energy interaction parameter $\varepsilon_{CO_2\text{-}Cu}$ approaches to 0.05 eV. This can be explained by

the fact that the number of CO_2 layers adsorbed on the solid surface is limited by applying a cutoff of non-bonded interaction. For the variation of density of CO_2 vapor with $\varepsilon_{CO_2\text{-}Cu}$, an opposite tendency can be seen in Figure 3f.

Condensation of CO_2 on the Cu-like surface for $\varepsilon_{CO_2\text{-}Cu} = 0.008$ eV is further studied. Initially, the stable droplet is vaporized at 273.15 K for a sufficient time of 50 ns under NVT (constant number of particles, constant volume, and constant temperature) ensemble. For the condensation simulation, a novel combination of MD simulation setups is adopted. The outmost layer of the Cu-like atoms is fixed to prevent the deformation of the solid surface. The inside two layers of the Cu-like atoms are simulated at 223.15 K under NVT ensemble as cooling source. MD simulations of the top outside three layers of Cu atoms and the CO_2 molecules are performed under NVE (constant number of particles, constant volume, and constant energy) ensemble for exchanging energy between CO_2 and the cooling layers. A long-enough simulation time of around 125 ns is assigned for mimicking the condensation process. The kinetics of the CO_2 condensation on the Cu-like surface is characterized by the analysis of the droplet size (molecular number). Figure 4a shows the variations in the number of liquid CO_2 molecules and the density of the vapor phase within the whole simulation time span. During vaporization (grey region), the droplet is fully vaporized at about 7 ns and the vaporization of the droplet becomes less pronounced as indicated by the reduction in $\frac{d\rho}{dt}$. From 7-50 ns, the system is mainly composed of CO_2 vapor contacting the Cu-like surface. In the curve of CO_2 condensation from 50-75 ns, the number of liquid CO_2 molecules rapidly increases to a constant in response to cooling (red curve of Figure 4a). Meanwhile, the density of CO_2 vapor decreases to a constant as a result of the law of conservation of mass. Both events quantitatively explain the CO_2 condensation on the Cu-like surface. Figure 4b plots the sum interaction forces between CO_2 molecules and the Cu-like surface in the three orthogonal directions. In the planar directions of the surface, the sum interaction forces oscillate around zero in both the vaporization and the condensation processes. In contrast, the average

total interaction force in the vertical (z) direction shows a similar tendency to the number of liquid CO_2 molecules. At complete vaporization, an average interaction force of around -2.8 eV/Å is yielded. At late phases of condensation, however, the system shows a mean interaction force of about -1.25 eV/Å. Such a difference is mainly attributed to the mean distance of the center of mass position between CO_2 and surface in the vertical direction.

To reveal the kinetic mechanism of cooling-induced CO_2 condensation, a series of top-viewed snapshots, in which gas molecules are removed, are captured at different condensation times as shown in Figure 4c. At 40 ns, no droplet is identified, indicating that the original droplet is completely vaporized. The condensation process of a CO_2 droplet on a Cu-like cooling surface is roughly divided into three stages. The first stage corresponds to the nucleation of CO_2 clusters as illustrated by the snapshot captured at 50.5 ns. It is observed that a large number of CO_2 clusters heterogeneously nucleate on the Cu-like cooling surface at the same time. This stage is a very rapid process. The second stage of the condensation process is primarily characterized by formation of droplets via coalescence and growth of CO_2 clusters as seen in snapshots captured from 52-66.3 ns. The nucleated CO_2 clusters dynamically form droplets by diffusion of CO_2 vapor molecules from the surroundings. CO_2 droplets are also formed by coalescence of nearby CO_2 clusters due to their strong non-bonded attractions. The droplet growth by coalescence does not increase the condensed mass of CO_2 on the Cu-like surface, in contrast to droplet growth by diffusion. Moreover, because the contacting area of the solid-surface is increased by the coalescence of neighboring nucleated clusters and droplets, fresh clusters or droplets grow by nucleation and diffusion. The final stage of the process is uniquely characterized by Ostwald ripening-coalescence mechanisms of CO_2 droplets. This stage lasts from around 66.7- 175 ns. The long-plateau characteristic in the curves of Figure 4a indicates that there is no growth of droplet by diffusion of CO_2 molecules from the vapor. As a result of the Ostwald ripening and coalescence behaviour, a single stable droplet finally condenses on the cooling Cu-like surface within

approximately 174 ns. During the whole condensation process, the condensed droplets show higher potential energy at the surface than in the interior due to the surface effect.

To gain more insights into the Ostwald ripening behaviour during the CO_2 condensation process, the two large condensed droplets on the Cu-like surface at the final stage are further characterized. Figure 5a monitors the numbers of CO_2 molecules (N_1 and N_2) in droplet #1 and droplet #2, as well as the sum number of liquid CO_2 molecules (N). The two condensed droplets show an opposite trend in the sum of the molecules. The sum of the molecules N_1 in droplet #1 almost increases linearly from around 14000 to 20000 with increasing condensation time, whereas in case of droplet #2 it decreases linearly from about 9000 to 3500 within the same time. By linearly fitting the curves, the corresponding growth rate and reduction rate of the two droplets are determined to be around 54 and 53 molecules/ns, respectively. Although there exists great variation in the sum of the CO_2 molecules in both droplets, the total number of liquid molecules remains constant. To quantitatively explain the molecular exchanges between the two-condensed droplets, the CO_2 molecules in droplet #1 at 66.5 ns are specifically marked and traced. Figure 5b shows the sums of marked CO_2 molecules in both droplets (n_1 and n_2) as a function of condensation time. The sum of marked molecules n_1 (n_2) monotonically decreases (increases) with time. Interestingly, the variation rates of n_1 and n_2, however, are condensation time dependent. A steep drop (rise) in n_1 (n_2) from around 9000 to 2000 (0 to 3000) within approximately 6.0 ns is identified. Soon afterwards, a nearly linear increase (decrease) in n_1 (n_2) is found. A constant variation rate of around 11 molecules/ns for both n_1 and n_2 is determined by fitting the linear part of the curves in the late phase, which is around 3-fold smaller than the growth rate of droplet #1 and the decay rate of droplet #2, respectively. Moreover, to further reveal the Ostwald ripening-coalescence mechanisms for CO_2 condensation on the Cu-like surface, a set of snapshots, in which the two condensed droplets are purple- and yellow-colored, captured at different times (from 66.5 to 168.5 ns) are shown in Figure 5c. Besides the size change of droplets by molecular exchange and diffusion, it is observed that both droplets migrate on the Cu-like smooth surface when one droplet

is far from the other. As the distance between condensed droplets becomes critical, droplets rapidly coalesce due to their attractive interaction forces. As a consequence, a single droplet with constant size finally condensed on the Cu-like surface. This suggests that the distance between droplets is a critical parameter to determine the Ostwald ripening and coalescence mechanisms during the CO_2 condensation. It is also found that the marked CO_2 molecules are homogeneously distributed in the droplets during the condensation process. This indicates that the molecules in the droplets are able to rapidly diffuse from the interior to the surface and also to the zone of CO_2 vapor.

4. Conclusions

In summary, contact angle and dropwise condensation of water on different solid surfaces have been subjected to extensive research. By designing the solid surface structures, dropwise condensation of water vapor can be achieved for water collection. However, as far as we know, literature on a solid surface for dropwise CO_2 condensation is virtually non-existing. In this study, classic MD simulations with accurate forcefields are performed to investigate the condensation and the contact angle of a CO_2 droplet on a Cu-like solid surface for CO_2 capture. Depending on the wettability of the Cu-like surface, either dropwise or filmwise condensation of CO_2 is achieved. For droplet condensation on the macroscale, there exists a transition from CO_2-phobic to CO_2-philic at a critical energy interaction parameter of $\varepsilon_{CO_2\text{-}Cu} = 0.009$ eV (corresponding to a liquid-solid tension of approximately 10 mN/m); however, the sum of condensed CO_2 molecules on a solid surface is insensitive to the energy interaction parameter $\varepsilon_{CO_2\text{-}Cu}$. For filmwise condensation, the sum of condensed CO_2 molecules significantly increases as the energy interaction parameter $\varepsilon_{CO_2\text{-}Cu}$ increases from 0.012 to 0.050 eV, but remains constant with further increase of $\varepsilon_{CO_2\text{-}Cu}$. Condensation of a CO_2 droplet on a Cu-like surface exhibits three distinct stages. In the first stage, heterogeneous nucleation of clusters is dominant and the nucleation rate is fairly fast. The second stage of condensation is primarily characterized by cluster growth to droplets via diffusion-coalescence mechanisms. The large-scale coalescence of

clusters as droplets arises from cluster diffusion and strong attraction between short-distanced neighboring clusters. Finally, a combination of Ostwald ripening in which one droplet continues to grow as function of time (~ t) while the other simultaneously decreases as function of time (~ t), and the coalescence mainly dominates in the last stage of the condensation process. Considerable molecular exchange between droplets occurs via fast diffusion. These results provide guidance for the design of functionalized surfaces to promote dropwise condensation of CO_2, as well as insight into the condensation behaviour that will occur on such surfaces

Acknowledgments

This work is financially supported by the Research Council of Norway (RCN) through the CLIMIT program project NanoDrop (Grant No. 254813), the National Natural Science Foundation of China (Grant Nos. 11772278 and 11502221), the Fundamental Research Funds for the Central Universities (Xiamen University: Grant Nos. 20720180014, 20720180018 and 20720160088), Fujian Provincial Department of Science & Technology (2017J05028), Doctoral Fund of the Ministry of Education (20130121110018), "111" Project (B16029) and the 1000 Talents Program from Xiamen University. The computational resources are provided by the Norwegian Metacenter for Computational Science (NOTUR NN9110K and NN9391K).

References

1. Meylan, F. D.; Moreau, V.; Erkman, S., CO_2 Utilization in the Perspective of Industrial Ecology, an Overview. *Journal of CO_2 Utilization* **2015**, *12*, 101-108.

2. Song, C., Global Challenges and Strategies for Control, Conversion and Utilization of CO_2 for Sustainable Development Involving Energy, Catalysis, Adsorption and Chemical Processing. *Catalysis Today* **2006**, *115*, 2-32.

3. Hunt, A. J.; Sin, E. H. K.; Marriott, R.; Clark, J. H., Generation, Capture, and Utilization of Industrial Carbon Dioxide. *ChemSusChem* **2010**, *3*, 306-322.

4. Huang, C.-H.; Phan, D. t.; Tan, C.-S., CO_2 Utilization. In *Handbook of Industrial Chemistry and Biotechnology*, Kent, J. A.; Bommaraju, T. V.; Barnicki, S. D., Eds. Springer International Publishing: Cham, 2017; pp 1781-1802.

5. Alper, E.; Orhan, O. Y., CO_2 Utilization: Developments in Conversion Processes. *Petroleum* **2017**, *3*, 109-126.

6. Li, L.; Zhao, N.; Wei, W.; Sun, Y., A Review of Research Progress on CO_2 Capture, Storage, and Utilization in Chinese Academy of Sciences. *Fuel* **2013**, *108*, 112-130.

7. Yu, K. M. K.; Curcic, I.; Gabriel, J.; Tsang, S. C. E., Recent Advances in CO_2 Capture and Utilization. *ChemSusChem* **2008**, *1*, 893-899.

8. Rubin, E. S.; Davison, J. E.; Herzog, H. J., The Cost of CO_2 Capture and Storage. *International Journal of Greenhouse Gas Control* **2015**, *40*, 378-400.

9. Leung, D. Y. C.; Caramanna, G.; Maroto-Valer, M. M., An Overview of Current Status of Carbon Dioxide Capture and Storage Technologies. *Renewable and Sustainable Energy Reviews* **2014**, *39*, 426-443.

10. Vitillo, J. G.; Smit, B.; Gagliardi, L., Introduction: Carbon Capture and Separation. *Chemical Reviews* **2017**, *117*, 9521-9523.

11. Figueroa, J. D.; Fout, T.; Plasynski, S.; McIlvried, H.; Srivastava, R. D., Advances in CO_2 Capture Technology—the U.S. Department of Energy's Carbon Sequestration Program. *International Journal of Greenhouse Gas Control* **2008**, *2*, 9-20.

12. Kanniche, M.; Gros-Bonnivard, R.; Jaud, P.; Valle-Marcos, J.; Amann, J.-M.; Bouallou, C., Pre-Combustion, Post-Combustion and Oxy-Combustion in Thermal Power Plant for CO_2 Capture. *Applied Thermal Engineering* **2010**, *30*, 53-62.

13. Wang, M.; Lawal, A.; Stephenson, P.; Sidders, J.; Ramshaw, C., Post-Combustion CO_2 Capture with Chemical Absorption: A State-of-the-Art Review. *Chemical Engineering Research and Design* **2011**, *89*, 1609-1624.

14. Mondal, M. K.; Balsora, H. K.; Varshney, P., Progress and Trends in CO_2 Capture/Separation Technologies: A Review. *Energy* **2012**, *46*, 431-441.

15. Olajire, A. A., CO_2 Capture and Separation Technologies for End-of-Pipe Applications – a Review. *Energy* **2010**, *35*, 2610-2628.

16. Spigarelli, B. P.; Kawatra, S. K., Opportunities and Challenges in Carbon Dioxide Capture. *Journal of CO_2 Utilization* **2013**, *1*, 69-87.

17. Kadoura, A.; Narayanan Nair, A. K.; Sun, S., Molecular Simulation Study of Montmorillonite in Contact with Variably Wet Supercritical Carbon Dioxide. *The Journal of Physical Chemistry C* **2017**, *121*, 6199-6208.

18. Romanov, V.; Soong, Y.; Carney, C.; Rush, G. E.; Nielsen, B.; O'Connor, W., Mineralization of Carbon Dioxide: A Literature Review. *ChemBioEng Review* **2015**, *2*, 231-256.

19. Klemm, O., Schemenauer, R. S., Lummerich, A., Cereceda, P., Marzol, V., Corell, D., van Heerden, J., Reinhard, D., Gherezghiher, T., Olivier, J., et al., Fog as a Fresh-Water Resource: Overview and Perspectives. *Ambio* **2012**, *41*, 221-234.

20. Fessehaye, M.; Abdul-Wahab, S. A.; Savage, M. J.; Kohler, T.; Gherezghiher, T.; Hurni, H., Fog-Water Collection for Community Use. *Renewable & Sustainable Energy Reviews* **2014**, *29*, 52-62.

21. Domen, J. K.; Stringfellow, W. T.; Camarillo, M. K.; Gulati, S., Fog Water as an Alternative and Sustainable Water Resource. *Clean Technologies and Environmental Policy* **2014**, *16*, 235-249.

22. Khalil, B.; Adamowski, J.; Shabbir, A.; Jang, C.; Rojas, M.; Reilly, K.; Ozga-Zielinski, B., A Review: Dew Water Collection from Radiative Passive Collectors to Recent Developments of Active Collectors. *Sustainable Water Resources Management* **2016**, *2*, 71-86.

23. Snustad, I.; Røe, I. T.; Brunsvold, A.; Ervik, Å.; He, J.; Zhang, Z., A Review on Wetting and Water Condensation - Perspectives for CO_2 condensation. *Advances in Colloid and Interface Science* **2018**, *256*, 291-304.

24. Schaef, H. T.; Glezakou, V. A.; Owen, A. T.; Ramprasad, S.; Martin, P. F.; McGrail, B. P., Surface Condensation of CO_2 onto Kaolinite. *Environmental Science & Technology Letters* **2014**, *1*, 142-145.

25. Chen, C.; Wan, J.; Li, W.; Song, Y., Water Contact Angles on Quartz Surfaces under Supercritical CO_2 Sequestration Conditions: Experimental and Molecular Dynamics Simulation Studies. *International Journal of Greenhouse Gas Control* **2015**, *42*, 655-665.

26. Chen, C.; Chai, Z.; Shen, W.; Li, W.; Song, Y., Wettability of Supercritical CO_2–Brine–Mineral: The Effects of Ion Type and Salinity. *Energy & Fuels* **2017**, *31*, 7317-7324.

27. Liang, Y.; Tsuji, S.; Jia, J.; Tsuji, T.; Matsuoka, T., Modeling CO_2–Water–Mineral Wettability and Mineralization for Carbon Geosequestration. *Accounts of Chemical Research* **2017**, *50*, 1530-1540.

28. Chen, C.; Dong, B.; Zhang, N.; Li, W.; Song, Y., Pressure and Temperature Dependence of Contact Angles for CO_2/Water/Silica Systems Predicted by Molecular Dynamics Simulations. *Energy & Fuels* **2016**, *30*, 5027-5034.

29. Chen, C.; Zhang, N.; Li, W.; Song, Y., Water Contact Angle Dependence with Hydroxyl Functional Groups on Silica Surfaces under CO_2 Sequestration Conditions. *Environmental Science & Technology* **2015**, *49*, 14680-14687.

30. Javanbakht, G.; Sedghi, M.; Welch, W.; Goual, L., Molecular Dynamics Simulations of CO_2/Water/Quartz Interfacial Properties: Impact of CO_2 Dissolution in Water. *Langmuir* **2015**, *31*, 5812-5819.

31. Iglauer, S.; Mathew, M. S.; Bresme, F., Molecular Dynamics Computations of Brine– CO_2 Interfacial Tensions and Brine–CO_2–Quartz Contact Angles and Their Effects on Structural and Residual Trapping Mechanisms in Carbon Geo-Sequestration. *Journal of Colloid and Interface Science* **2012**, *386*, 405-414.

32. Jung, J.-W.; Wan, J., Supercritical CO_2 and Ionic Strength Effects on Wettability of Silica Surfaces: Equilibrium Contact Angle Measurements. *Energy & Fuels* **2012**, *26*, 6053-6059.

33. Liu, S.; Yang, X.; Qin, Y., Molecular Dynamics Simulation of Wetting Behavior at CO_2/Water/Solid Interfaces. *Chinese Science Bulletin* **2010**, *55*, 2252-2257.

34. Niu, D.; Tang, G. H., The Effect of Surface Wettability on Water Vapor Condensation in Nanoscale. *Scientific Reports* **2016**, *6*, 19192.

35. Gao, S.; Liao, Q.; Liu, W.; Liu, Z., Effects of Solid Fraction on Droplet Wetting and Vapor Condensation: A Molecular Dynamic Simulation Study. *Langmuir* **2017**, *33*, 12379-12388.

36. Ou, X.; Wang, X.; Lin, Z.; Li, J., Heterogeneous Condensation of Water on the Mica (001) Surface: A Molecular Dynamics Simulation Work. *The Journal of Physical Chemistry C* **2017**, *121*, 6813-6819.

37. Hong, S. D.; Ha, M. Y.; Balachandar, S., Static and Dynamic Contact Angles of Water Droplet on a Solid Surface Using Molecular Dynamics Simulation. *Journal of Colloid and Interface Science* **2009**, *339*, 187-195.

38. Hirvi, J. T.; Pakkanen, T. A., Wetting of Nanogrooved Polymer Surfaces. *Langmuir* **2007**, *23*, 7724-7729.

39. Šolc, R.; Tunega, D.; Gerzabek M., H.; Woche S., K.; Bachmann, J., Wettability of Organically Coated Tridymite Surface – Molecular Dynamics Study. In *Pure and Applied Chemistry*, **2015**; Vol. 87, p 405.

40. Andrews, J. E.; Sinha, S.; Chung, P. W.; Das, S., Wetting Dynamics of a Water Nanodrop on Graphene. *Physical Chemistry Chemical Physics* **2016**, *18*, 23482-23493.

41. W. Xu; Z. Lan; B. L. Peng; R. F. Wen; Ma, X. H., Effect of Surface Free Energies on the Heterogeneous Nucleation of Water Droplet: A Molecular Dynamics Simulation Approach. *The Journal of Chemical Physics* **2015**, *142*, 054701.

42. Koishi, T.; Yasuoka, K.; Fujikawa, S.; Ebisuzaki, T.; Zeng, X. C., Coexistence and Transition between Cassie and Wenzel State on Pillared Hydrophobic Surface. *Proceedings of the National Academy of Sciences* **2009**, *106*, 8435-8440.

43. Mishin, Y.; Mehl, M. J.; Papaconstantopoulos, D. A.; Voter, A. F.; Kress, J. D., Structural Stability and Lattice Defects in Copper: Ab Initio, Tight-Binding, and Embedded-Atom Calculations. *Physical Review B* **2001**, *63*, 224106.

44. Daw, M. S.; Baskes, M. I., Embedded-Atom Method: Derivation and Application to Impurities, Surfaces, and Other Defects in Metals. *Physical Review B* **1984**, *29*, 6443-6453.

45. Avendaño, C.; Lafitte, T.; Galindo, A.; Adjiman, C. S.; Jackson, G.; Müller, E. A., Saft-Γ Force Field for the Simulation of Molecular Fluids. 1. A Single-Site Coarse Grained Model of Carbon Dioxide. *The Journal of Physical Chemistry B* **2011**, *115*, 11154-11169.

46. J. E. Jones; Sc., D., On the Determination of Molecular Fields. — II. From the Equation of State of a Gas. *Proceedings of the Royal Society of London. Series A* **1924**, *106*, 463-477.

47. C. A. Leng; J. S. Rowlinson; F. R. S.; Thompson, S. M., The Gas – Liquid Surface of the Penetrable Sphere Model. *Proceedings of the Royal Society of London. A. Mathematical and Physical Sciences* **1976**, *352*, 1-23.

48. Weeks, J. D., Structure and Thermodynamics of the Liquid–Vapor Interface. *The Journal of Chemical Physics* **1977**, *67*, 3106-3121.

49. Wilhelmsen, Ø.; Aasen, A.; Skaugen, G.; Aursand, P.; Austegard, A.; Aursand, E.; Gjennestad, M. A.; Lund, H.; Linga, G.; Hammer, M., Thermodynamic Modeling with Equations of State: Present Challenges with Established Methods. *Industrial & Engineering Chemistry Research* **2017**, *56*, 3503-3515.

50. Roland Span; Wagner, W., A New Equation of State for Carbon Dioxide Covering the Fluid Region from the Triple-Point Temperature to 1100 K at Pressures up to 800 Mpa. *Journal of Physical and Chemical Reference Data* **1996**, *25*, 1509-1596.

51. Müller, E. A.; Jackson, G., Force-Field Parameters from the Saft-γ Equation of State for Use in Coarse-Grained Molecular Simulations. *Annual Review of Chemical and Biomolecular Engineering* **2014**, *5*, 405-427.

52. Hoang, H.; Delage-Santacreu, S.; Galliero, G., Simultaneous Description of Equilibrium, Interfacial, and Transport Properties of Fluids Using a Mie Chain Coarse-Grained Force Field. *Industrial & Engineering Chemistry Research* **2017**, *56*, 9213-9226.

Figures and Captions

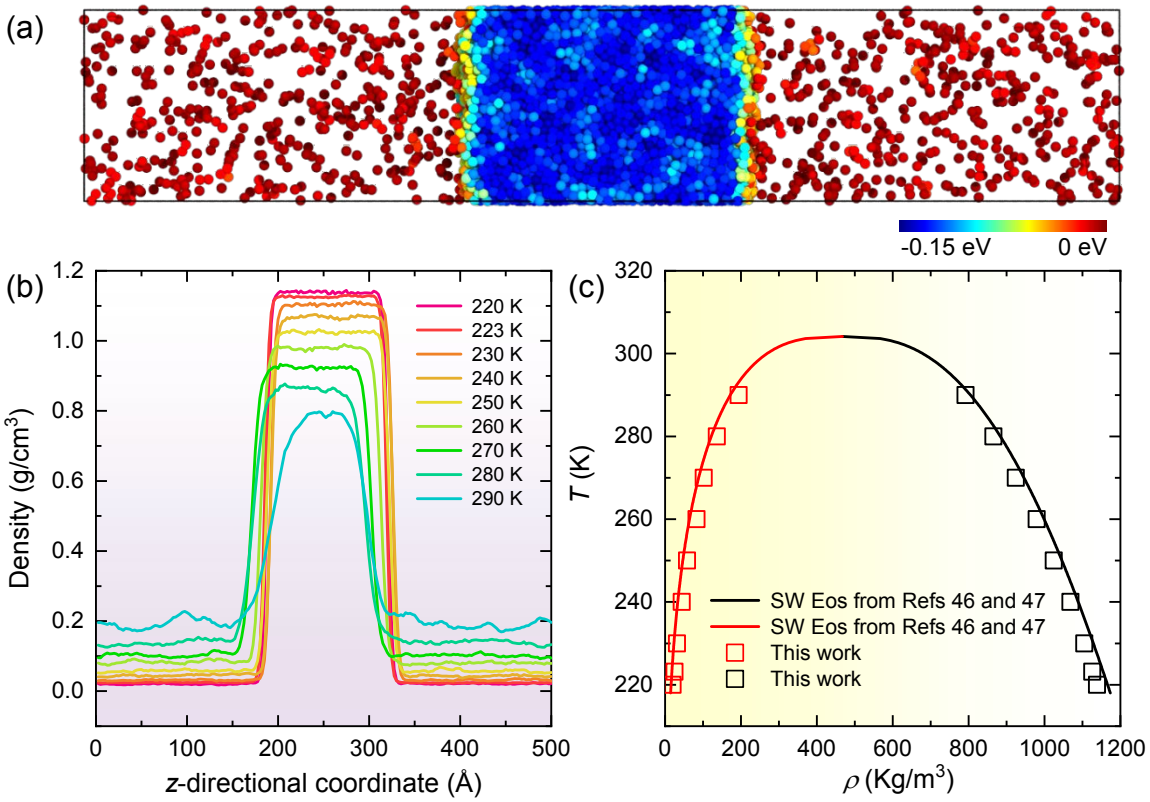

Figure 1 CO_2 vapor-liquid system. (a) A representative side-viewed snapshot of vapor-liquid coexistence of CO_2 in a box with dimensions of 92 × 92 × 500 Å^3. Molecular coarse-grained (CG) beads are colored on the basis of their potential energies for enhanced visibility. (b) Density profiles of the vapor-liquid equilibrium at temperatures varying from 220 K to 290 K. (c) Comparison of temperature-density of vapor-liquid coexistence of CO_2 with equilibrium of state (EoS) data [46-47].

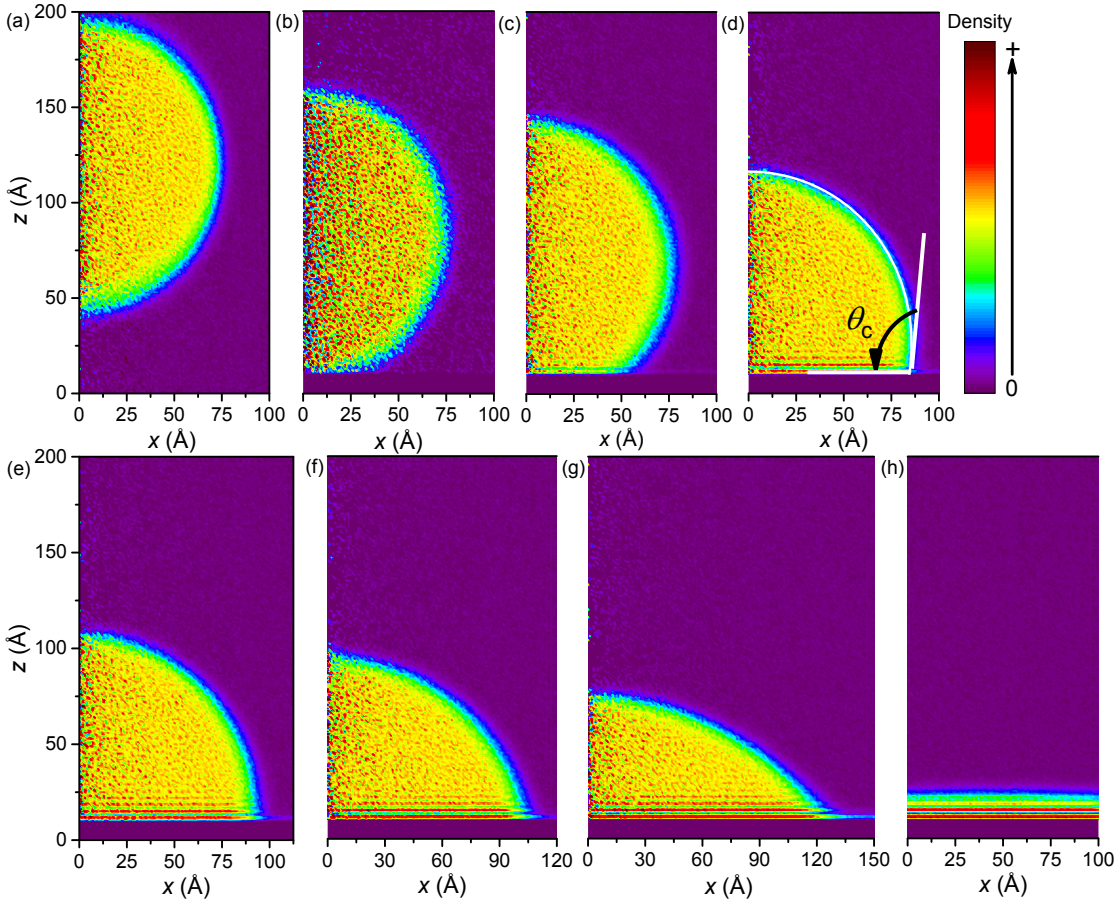

Figure 2 Relative density maps of CO_2 droplets on a Cu-like solid surface with a CO_2-surface interaction parameter $\varepsilon_{CO_2\text{-}Cu}$ of (a) 0.001 eV, (b) 0.003 eV, (c) 0.005 eV, (d) 0.008 eV, (e) 0.009 eV, (f) 0.01 eV, (g) 0.012 eV, and (h) 0.015 eV, respectively.

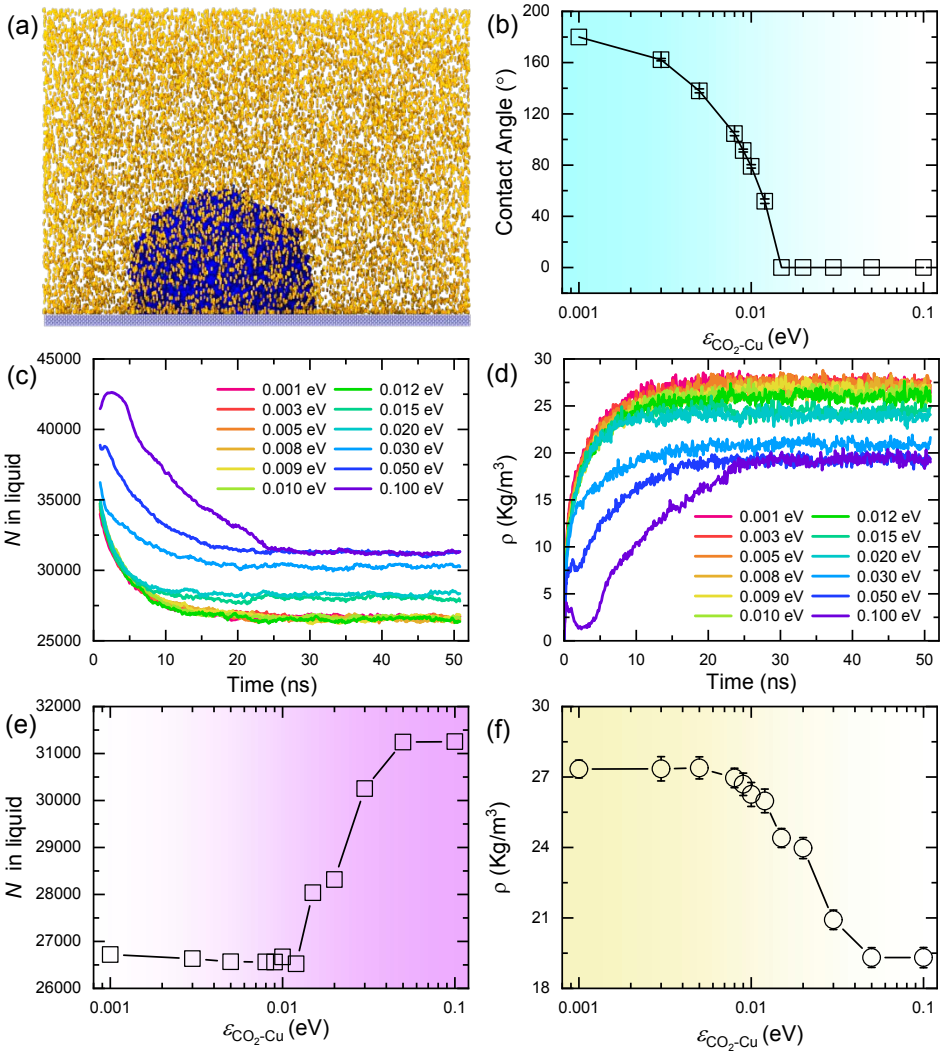

Figure 3 CO_2-solid surface-system analysis. (a) A snapshot of a CO_2 droplet and vapor contacting with Cu-like surface having an energy interaction parameterof $\varepsilon_{CO_2\text{-}Cu} = 0.008$ eV in equilibrium. Vaporized and liquid CO_2 molecules are yellow- and blue-highlighted for clarification, respectively. (b) Contact angle of CO_2 droplet as a function of interaction energy $\varepsilon_{CO_2\text{-}Cu}$. (c) and (d) Variation in number of liquid-state CO_2 and the density of the gas phase with the MD simulation time, respectively. (e) and (f) Variation in number of liquid-state CO_2 and the density of the gas phase with $\varepsilon_{CO_2\text{-}Cu}$, respectively.

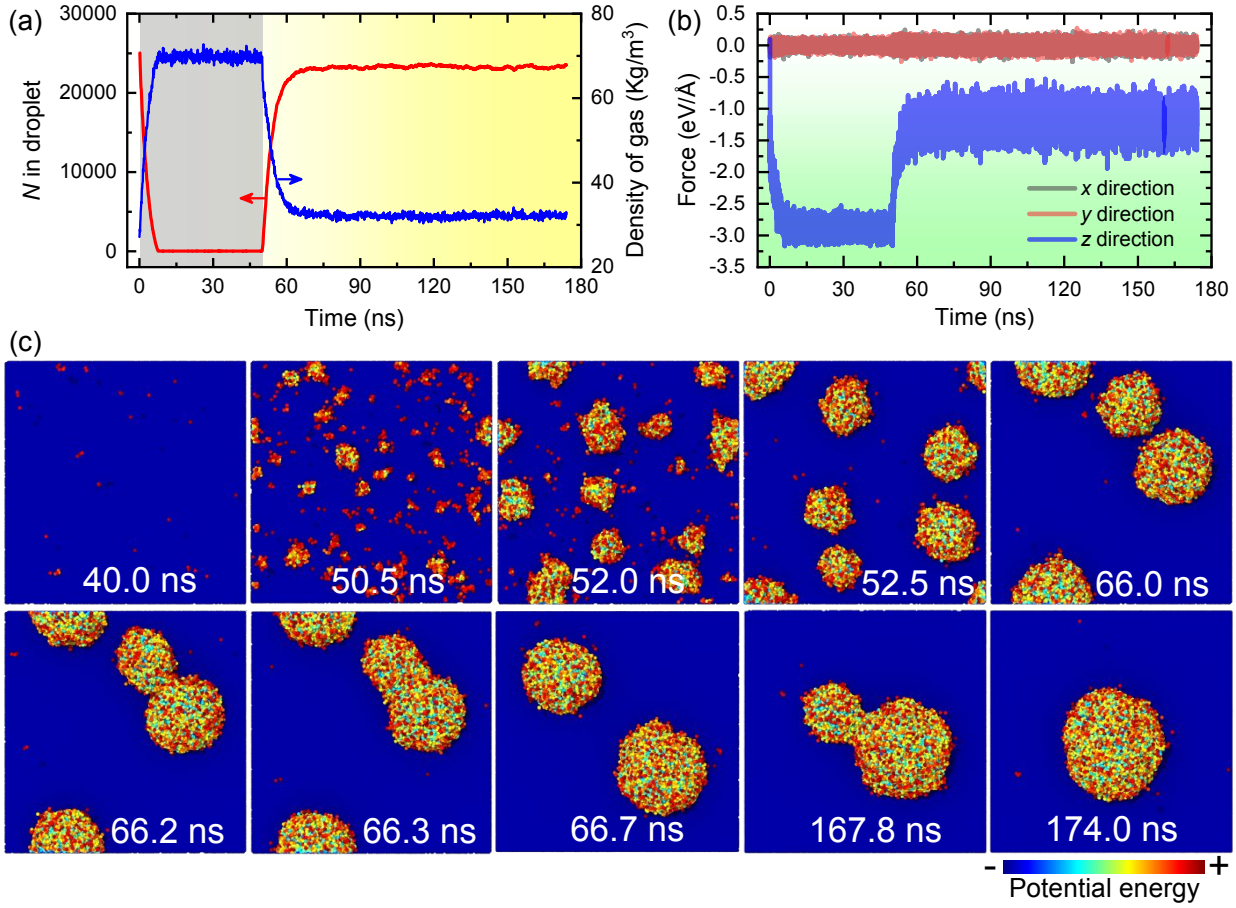

Figure 4 Analysis of vaporization and condensation of a CO_2 droplet on a Cu-like solid surface with an interaction $\varepsilon_{CO_2\text{-}Cu} = 0.008$ eV. (a) Number of CO_2 molecules in the droplet and the density of CO_2 gas phase as a function of MD simulation time. (b) Total interaction forces between CO_2 and Cu-like solid surface against MD simulation time along the three orthogonal directions. (c) Snapshots of the condensation process of CO_2 droplet on a cooling Cu-like solid surface. CG beads in the condensed droplet are colored according to their potential energies. CG gas beads that have potential energies > -0.05 eV are removed for enhanced visibility.

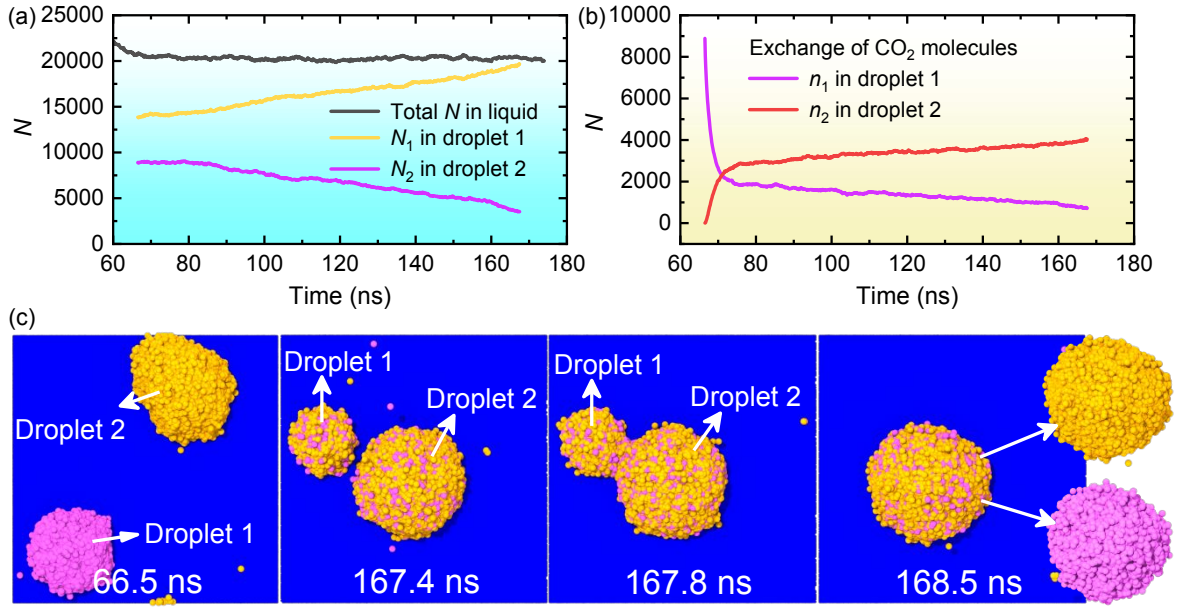

Figure 5 Condensation characteristics of a CO_2 droplet on a Cu-like solid surface. (a) Variations in number (N_1, N_2) of CO_2 molecules of two droplets and their total number (N) of CO_2 molecules with MD condensation time. (b) Exchange of CO_2 molecules between two droplets during the condensation process. (c) A sequence of snapshots illustrating the molecular exchange between two condensed droplets and Ostwald ripening and coalescence of two condensed CO_2 droplets during the condensation process. Coarse-grained (CG) beads of CO_2 in gas state are removed for clarification. For enhanced visualization of the exchange of CO_2 molecules, the two condensed CO_2 droplets on the Cu-like surface are purple- and yellow-highlighted, respectively. At the condensation time 168.5 ns, a droplet formed by coalescence of two droplets is composed of purple- and yellow-colored CO_2 molecules, explaining the molecular exchange during the condensation process. Particularly, purple- and yellow-colored CO_2 molecules (indicated by the arrows) are taken out from the formed droplet for showing the homogeneous distribution.

TOC graphic